Topographic organization in the auditory brainstem of juvenile mice is disrupted in congenital deafness

Richardson N. Leao[1], Hong Sun[2], Katarina Svahn[1], Amy Berntson[1], Monique Youssoufian[1], Antonio G. Paolini[3], Robert E. W. Fyffe[2] and Bruce Walmsley[1]

[1]*Synapse and Hearing Laboratory, The John Curtin School of Medical Research, The Australian National University, Canberra, ACT, Australia*
[2]*Department of Neuroscience, Cell Biology and Physiology, Wright State University, Dayton, OH, USA*
[3]*Latrobe University, Melbourne, VIC, Australia*

There is an orderly topographic arrangement of neurones within auditory brainstem nuclei based on sound frequency. Previous immunolabelling studies in the medial nucleus of the trapezoid body (MNTB) have suggested that there may be gradients of voltage-gated currents underlying this tonotopic arrangement. Here, our electrophysiological and immuno-labelling results demonstrate that underlying the tonotopic organization of the MNTB is a combination of medio-lateral gradients of low-and high-threshold potassium currents and hyperpolarization-activated cation currents. Our results also show that the intrinsic membrane properties of MNTB neurones produce a topographic gradient of time delays, which may be relevant to sound localization, following previous demonstrations of the importance of the timing of inhibitory input from the MNTB to the medial superior olive (MSO). Most importantly, we demonstrate that, in the MNTB of congenitally deaf mice, which exhibit no spontaneous auditory nerve activity, the normal tonotopic gradients of neuronal properties are absent. Our results suggest an underlying mechanism for the observed topographic gradient of neuronal firing properties in the MNTB, show that an intrinsic neuronal mechanism is responsible for generating a topographic gradient of time-delays, and provide direct evidence that these gradients rely on spontaneous auditory nerve activity during development.

Auditory nuclei in the mammalian brainstem are characterized by a high degree of order (Friauf & Lohmann, 1999; McAlpine *et al.* 2001; Rubel & Fritzsch, 2002; Yin, 2002; Mauk & Buonomano, 2004). In the medial nucleus of the trapezoid body (MNTB), neurones are topographically organized along a medio-lateral axis with the most medially located cells responding best to high sound frequencies, progressively changing to lower characteristic frequencies in the most lateral cells. An important question is 'what are the underlying mechanisms responsible for the progressive difference in neuronal firing properties along the tonotopic axis in a nucleus such as the MNTB?'. Previous studies have provided immunohistochemical evidence for a topographic arrangement of the expression of specific high-threshold potassium channels in the MNTB (Li *et al.* 2001; von Hehn *et al.* 2004). Li *et al.* (2001) demonstrated that Kv3.1 immunoreactivity in rat MNTB neurones is greater in the most medial neurones, which respond best to high-frequency tones. Surprisingly,

there is very little electrophysiological information on topographical differences in the membrane mechanisms underlying differences in the firing properties of neurones in auditory nuclei, including the MNTB (Barnes-Davies *et al.* 2004; von Hehn *et al.* 2004). Barnes-Davies *et al.* (2004) demonstrated that in the rat lateral superior olive (LSO), there is a gradient of low-threshold potassium currents, with lower characteristic frequency neurones exhibiting larger current amplitudes and stronger expression of Kv1.1 channels. A very recent study (Brew & Forsythe, 2005) has demonstrated a tonotopic gradient of total outward potassium currents in the rat MNTB, with medial neurones exhibiting larger currents than lateral neurones.

In the present study, we have used patch-clamp recordings of mouse MNTB neurones in brainstem slices to demonstrate the existence of topographic gradients of several voltage-gated currents, including low- and high-threshold potassium currents and

hyperpolarization-activated currents. The magnitude of some of these currents increases and of others decreases along the medio-lateral axis. Parallel immuno-histochemical analyses reveal topographic gradients of specific channel subunits that may underlie these currents. We then examined the question of how these topographic gradients are established. Auditory nerve activity may play a role, and previous studies have provided evidence for activity-dependent regulation of Kv1.1 and Kv3.1 channels in the avian nucleus magnocellularis following removal of the cochlea (Lu *et al.* 2004), and Kv3.1 expression is also disrupted in hearing-impaired mice (von Hehn *et al.* 2004). Auditory nerves exhibit spontaneous activity even before ear canal opening and the onset of sound-evoked activity, and it is therefore important to separate the effects of spontaneous and evoked auditory nerve activity in generating or modifying tonotopic maps (Friauf & Lohmann, 1999; Rubel & Fritzsch, 2002). In the present study we have made use of a congenitally deaf mouse (*dn/dn*, Bock *et al.* 1982; Keats & Berlin, 1999; Oleskevich *et al.* 2004; Leao *et al.* 2004*a*,*b*) in which there is no spontaneous auditory nerve activity prior to (or following) opening of the ear canal. Our results show that the normal topographic gradient of neuronal membrane properties is absent in these congenitally deaf mice, providing direct evidence that spontaneous auditory nerve activity plays an important role in tonotopic map formation during development.

Methods

Normal (CBA) and congenitally deaf (*dn/dn* with CBA background), 12–14 days postnatal mice were decapitated (for electrophysiology) or killed with an overdose of sodium pentobarbital according to the Australian National University Animal Ethics Committee and Wright State University IACUC protocols.

Electrophysiology

The forebrain and cerebellum were removed and placed in ice-cold low-calcium ACSF (mM: 130 NaCl, 3.0 KCl, 5.0 $MgCl_2$, 1.0 $CaCl_2$, 1.25 NaH_2PO_4, 26.2 $NaHCO_3$, 10 glucose, equilibrated with 95% O_2–5% CO_2). Transverse slices (200 μm) were made of the medial nucleus of the trapezoid body (MNTB) using an oscillating tissue slicer (Integraslice). Slices were incubated for 1 h in normal ACSF (mM: 130 NaCl, 3.0 KCl, 1.3 Mg_2SO_4, 2.0 $CaCl_2$, 1.25 NaH_2PO_4, 26.2 $NaHCO_3$, 10 glucose, equilibrated with 95% O_2–5% CO_2) at 35°C and subsequently held at room temperature (22–25°C) for electrophysiological recording. Some experiments were carried out at 35°C to examine the effects at a more physiological temperature. For assessing high-threshold

voltage-dependent K^+ currents, 1–3 mM TEA was added to the perfusate (containing also 1 μM TTX, 50 μM $CdCl_2$). For experiments examining dendrotoxin (DTX)-sensitive currents, the following drugs were added to the perfusate: 1 μM TTX, 10 μM ZD7288 to block I_h, 50 μM $CdCl_2$, with and without 100 nM α-DTX. Hyperpolarization-activated currents were analysed from recordings with and without 10 μM ZD7288. For analysis, currents with blocking agents were subtracted from those without.

Neurobiotin (0.5%) or Alexa-488 was added to the internal solution in order to determine the position of the cell within the MNTB. Recorded cells were separated in three groups according to the precise position of the labelled cell as determined in photo-micrographs of the whole MNTB, which was delimited and divided into three zones: medial (medial cell – MC), intermediate (intermediate cell – IC) and lateral (lateral cell – LC). Whole-cell current-clamp and voltage-clamp recordings from visualized MNTB neurones were made using an Axopatch 1D or an Axoclamp 2A and Axograph data acquisition and analysis software (Axon Instruments, San Francisco, California, USA). Access resistance (2.5–5.0 MΩ) was routinely compensated by > 80%. Patch-electrodes for current-clamp and voltage-clamp recordings contained (mM): (122.5 potassium gluconate, 17.5 KCl, 9 NaCl, 1 $MgCl_2$, 10 Hepes, 3 Mg-ATP, 0.3 GTP-tris and 0.2 EGTA). The pH was adjusted to 7.2 using KOH, and the osmolarity, when necessary, adjusted to 290–300 mosmol l^{-1} with sorbitol. Several compounds (see above) were used to isolate ionic currents. Current and voltage steps were applied and analysed using Axograph and Matlab R13 (Mathworks). Current-clamp protocols were either long-duration 800 ms current steps from −50 to 400 pA (50 pA increments) or brief pulse trains with frequencies of 150, 300 and 600 Hz (0.5 ms duration, 2 nA amplitude). Voltage-clamp protocols were as follows: the cell was held at a resting potential of −60 mV, which was stepped to a holding pre-potential of −90 mV for 750 ms before the test voltage step. Test steps were then made to potentials of −70 to +40 mV (in increments of 5 mV) and the current responses measured. Alternatively, current responses were measured from a holding potential of −60 mV, during application of 1 s voltage steps from −130 to −60 mV in 5 mV increments. Synaptic currents were also simulated by dynamic clamp using a differential amplifier that computes two inputs according to the equation

$$I(t) = g(t)\,(V(t) - V_{rev})$$

where $g(t)$ is the conductance waveform, $V(t)$ is the membrane voltage read from the patch-amplifier V_m output, V_{rev} is the reversal potential from the synaptic current.

Membrane currents were also modelled using a Hodgkin-Huxley-like model. The MNTB cell model

consisted of an inactivating voltage Na^+ current, non-inactivating low and high-threshold voltage-dependent K^+ currents, a cationic hyperpolarizing-activated current and a non-specific leakage current. Model parameters for hyperpolarizing-activated current and the low- and high-threshold voltage-dependent K^+ currents were obtained from the recorded data.

Model details and parameters. Channel conductance and currents followed the relationship:

$$I = \bar{g}a^\lambda b(V - V_r); \quad a = m, n, o, u; \quad b = h$$

where $\bar{g}$ is the maximum conductance, a is the activation variable of λth order, b is the inactivation variable and V_r is the reversal potential. Changes in a and b were governed by the differential equation:

$$\dot{x} = (x_\infty - x)/\tau_x, \quad x = a, b$$

where x_∞ is the steady-state value and τ_x is the time constant. Steady-state variables are described by opening and closing rate constants α and β. Opening and closing rating constants where described for m, n, o as:

$$\alpha = C_\alpha(V + V_c)\big/\big(e^{-(V+V_c)/V_\alpha} - 1\big)$$

and

$$\beta = C_\beta e^{-(V - V_c)/V_\beta};$$

for u as:

$$\alpha = C_\alpha e^{-(V - V_c)/V_\alpha}$$

and

$$\beta = C_\beta\big/\big(e^{-(V + V_c)/V_\beta} - 1\big);$$

and for h as:

$$\alpha = 0.007e^{(V+60)/20}$$

and

$$\beta = 1\big/\big(1 + e^{(V+30)/10}\big).$$

For the K^+ currents and I_h, C_α, C_β, V_α, V_β and V_c were obtained by fitting the equation $x_\infty = \alpha/(\alpha + \beta)$ to Boltzmann relationships ($g/\bar{g}$ *versus* V) and/or $\tau_x = 1/(\alpha + \beta)$ to the relationship activation/deactivation time constants *versus* voltage. Datasets used to obtain currents/voltage dynamics were obtained from recordings in which the series resistance was $< 5\,\text{M}\Omega$ and resistance compensation was $> 80\%$. Voltage-gated currents consisted of a Na^+ (I_{Na}) current ($\bar{g} = \bar{g}_{Na}; a = m; \lambda = 3; b = h; V_r = V_{Na}$), two K^+ currents (I_{TEA} and I_{DTX}), a high-threshold TEA-sensitive current ($\bar{g} = \bar{g}_{TEA}; a = n; \lambda = 4; b = 1; V_r = V_K$) and a low-threshold DTX-sensitive current ($\bar{g} = \bar{g}_{DTX}; a = o; \lambda = 3; b = 1; V_r = V_K$) and a hyperpolarization-activated current ($\bar{g} = \bar{g}_h; a = u; \lambda = 1; b = 1; V_r = V_{Ih}$). C_α, C_β, V_α, V_β and V_c constants for m were, respectively: -0.1, 0.5, 1, 20, 49; for n: -0.0344, 0.92, 2×10^{-6}, 0.17, 40.6; for o (LC and IC): -0.019, 0.23, 0.1, 43.654, 55.324; for o (MC): -0.03, 0.24, 0.1, 40.32, 51.3; for u: 0.001, 0.021, 10, 0, 70. Membrane voltage was modelled by:

$$\dot{V} = (I_{Na} + I_{DTX} + I_{TEA} + I_h + I_L + I_{Syn} + I_{ST})/c,$$

with I_{ext} equal to the injected current; leakage, $I_L = g_L(V - V_L)$ and synaptic currents equal to $I_{Syn} = \bar{g}_{Syn}A(V - V_{Syn})$. $\bar{g}_{Syn}$ is the maximum synaptic conductance (50 nS for IPSCs and EPSCs) and V_{Syn} is the reversal potential for the synaptic current (-90 mV for IPSCs and 60 mV for EPSCs) and A is the activation/deactivation variable equal to $e^{-\tau_d/(t - t_{ON})}(1 - e^{-\tau_r/(t - t_{ON})})$. τ_d is the decay time, τ_r the rise time, and t_{ON} is the time when the PSC occurs. Conductance values ($\bar{g}_{Na}$, $\bar{g}_{TEA}$, $\bar{g}_{DTX}$, $\bar{g}_h$, g_L) for MC were, respectively (in nS): 247, 40, 11.2, 3.12 and 0.5; for IC: 237, 20, 8.2, 2.12, 1.5; for LC: 247, 10, 9.3, 0.92, 2.2.

In vivo auditory nerve activity recording

In vivo experiments were approved by La Trobe University Animal Research Ethics Committee (AEC03/13) in accordance with NH and MRC animal experimentation guidelines. Mice pups (CBA and *dn/dn*) were anaesthetized with intraperitoneal urethane in water (5% w/v: initial volume injected 0.1 ml) with administration of supplemental doses upon observation of pedal or corneal reflexes. The mouse pup was placed within a stereo-taxic frame with in-house modified ear bars and mouth piece. Body temperature was maintained by placing the mouse pups on a hot water bottle. An incision was made to expose the skull and following a craniotomy a portion of the cerebellum was aspirated to reveal the ventral cochlear nucleus (VCN). A 4 mm eight-channel (recording sites spaced 50 μm apart) single-shank Michigan silicon probe (University of Michigan Center for Neural Communication Technology) was inserted under visual control through the posterior aspects of the VCN at an angle to allow penetration into the auditory nerve (AN). This is a commonly used and less traumatic approach to access the AN as previously described in the rat (Paolini *et al.* 2001; Shepherd *et al.* 2004) and in the mouse (Taberner & Liberman, 2005). The probe was connected to a Medusa RA16 preamplifier with optic fibre link to a Medusa RA16BA Base Station (Tucker-Davis Technologies, Gainesville, FL, USA) and spontaneous single and multiunit activity recorded from the most apical electrodes deep from the point of penetration (400–600 μm). Spontaneous activity was sampled at 24 kHz using Open X software (Tucker-Davis Technologies, Gainesville, FL, USA). Recordings were initially conducted in the AN with control recordings

subsequently made in the intact cerebellum on the opposite side of the exposure.

Immunohistochemistry

Following killing, mice were perfused with cold vascular rinse (0.01 M phosphate buffer (PB) with 137 mM NaCl, 3.4 mM KCl and 6 mM NaHCO$_3$) followed by fixative (4% paraformaldehyde in 0.1 M phosphate buffer; pH 7.4) for 10–15 min. Transverse sections (30 μm thick) of the brainstem were obtained at the level of the MNTB on a freezing sliding microtome, washed in PB containing 0.1% Triton X-100 (PB-T) and then incubated overnight at 4°C with the following primary antibodies: Kv1.1 (Alomone, rabbit, 1 : 100), Kv1.2 (Upstate, mouse, 1 : 100), Kv3.1b (Exalpha, rabbit, 1 : 100 and Alomone, rabbit, 1 : 100), Kv3.4 (Alomone, rabbit, 1 : 100), HCN2 (Alomone, rabbit, 1 : 100) and HCN4 (Alomone, rabbit, 1 : 100), followed by incubation (3 h) in species-appropriate CY3-conjugated secondary antibody (Jackson, 1 : 50); for analysis of optical density of immunostaining, sections were processed with standard avidin–biotin complex (ABC; Vector) protocols, with diaminobenzidine (DAB) as chromogen, after incubation in the primary antibody. In these experiments, the experimental tissues (control and *dn/dn*) were processed identically (simultaneous incubation in the same antibody, ABC and DAB solutions) to avoid experiment-to-experiment variability. Photo-micrographic comparisons are shown only for tissue processed in the same batch. Sections were mounted on gelatin-coated slides and cover-slipped with or without fluorescence mounting medium.

Glutamatergic synaptic terminals were visualized with guinea pig or rabbit anti-VGLUT1 (Chemicon, 1 : 1000; Synaptic Systems, 1 : 1000) and cell bodies were visualized with FITC-conjugated fluorescent Nissl stain (1 : 100; Molecular Probes). Fluorescence images were collected using a laser scanning confocal microscope (Olympus Fluoview) with 20 ×, or 60 × oil immersion, objectives, digitally magnified 2–3 × at 1024 × 1024 pixel resolution. For intensity/optical density measurements of channel immunoreactivity, images of ABC reaction product in the MNTB were taken on an Olympus BX microscope using a spot RT digital camera (Diagnostic Instruments, USA). The resultant 8-bit images contained a grayscale of pixel intensities that ranged from 0 to 255, where 0 is white and 255 is black. To avoid differences in light intensity of the captured images, all images were digitised at the same light intensity in the microscope and the same exposure time in the software. Rather than imaging the whole nucleus and measuring total optical density, which will be complicated by any background staining, small defined areas of interest (AOI) were drawn manually to incorporate individual cell outlines or, separately, the presynaptic profiles immediately surrounding each cell. The average optical density of labelling in the respective AOIs was measured automatically using ImagePro Plus software 5.0 (Media Cybernetics, Silver Springs, Maryland, USA). AOI locations and respective optical density measurements were defined according to the three medio-lateral zones defined above.

Results

Patch-clamp recordings were successfully obtained from 130 MNTB neurones. The location of cells within the MNTB was determined by intracellular filling with neuro-biotin or Alexa labels. Figure 1*A* shows a transverse slice with two labelled MNTB neurones.

Tonotopic gradient of MNTB neurone firing properties in normal mice

The MNTB is organized tonotopically along a medio-lateral axis, with cells receiving input from the highest acoustic frequencies located most medially within the nucleus. We first investigated the response of MNTB neurones to current steps and trains of brief current pulses in relation to their medio-lateral location. Figure 1*C* shows examples of action potentials in response to current pulse trains (600 Hz), for a medially located cell (blue trace) and a lateral cell (red). It is evident that the lateral cell could not reliably generate an action potential for every current pulse, in contrast to the medial cell. Figure 1*D* shows summary data for 42 cells, indicating that medial cells exhibit a much lower failure rate than lateral cells (at 600 Hz, MC failure ratio ($22.4 \pm 5.0\%$) was lower than LC ($59 \pm 2.0\%$, $P < 0.01$, $n = 15$).

Whole-cell capacitance was used as a functional measure of cell size (membrane area). There was no difference in whole-cell capacitance between medial and lateral MNTB neurones (Fig. 1*D*, open bars; MC, 24.2 ± 1.0 pF; IC, 23.8 ± 1.2 pF; LC 23.2 ± 1.1 pF; $P > 0.05$). Next, we examined the firing responses of MNTB neurones to current steps of different amplitudes. Figure 1*E* shows that the delay in action potential generation for the same amplitude current step (150 pA) for a medial cell (blue trace) is much less than for a lateral cell (red trace). Figure 1*F* illustrates a plot of the location of cells within the MNTB according to the delay in action potential generation for the same amplitude current step (150 pA). This plot shows clearly that the most medial cells exhibit the shortest delays. These results demonstrate that the membrane properties of MNTB neurones vary systematically along the medio-lateral axis of the MNTB.

A series of experiments was carried out at a more physiological temperature (35°C) to investigate if the time delay gradient was significant at this temperature. Our results (see Supplemental Material) demonstrated that the delays were substantial and comparable to those at room
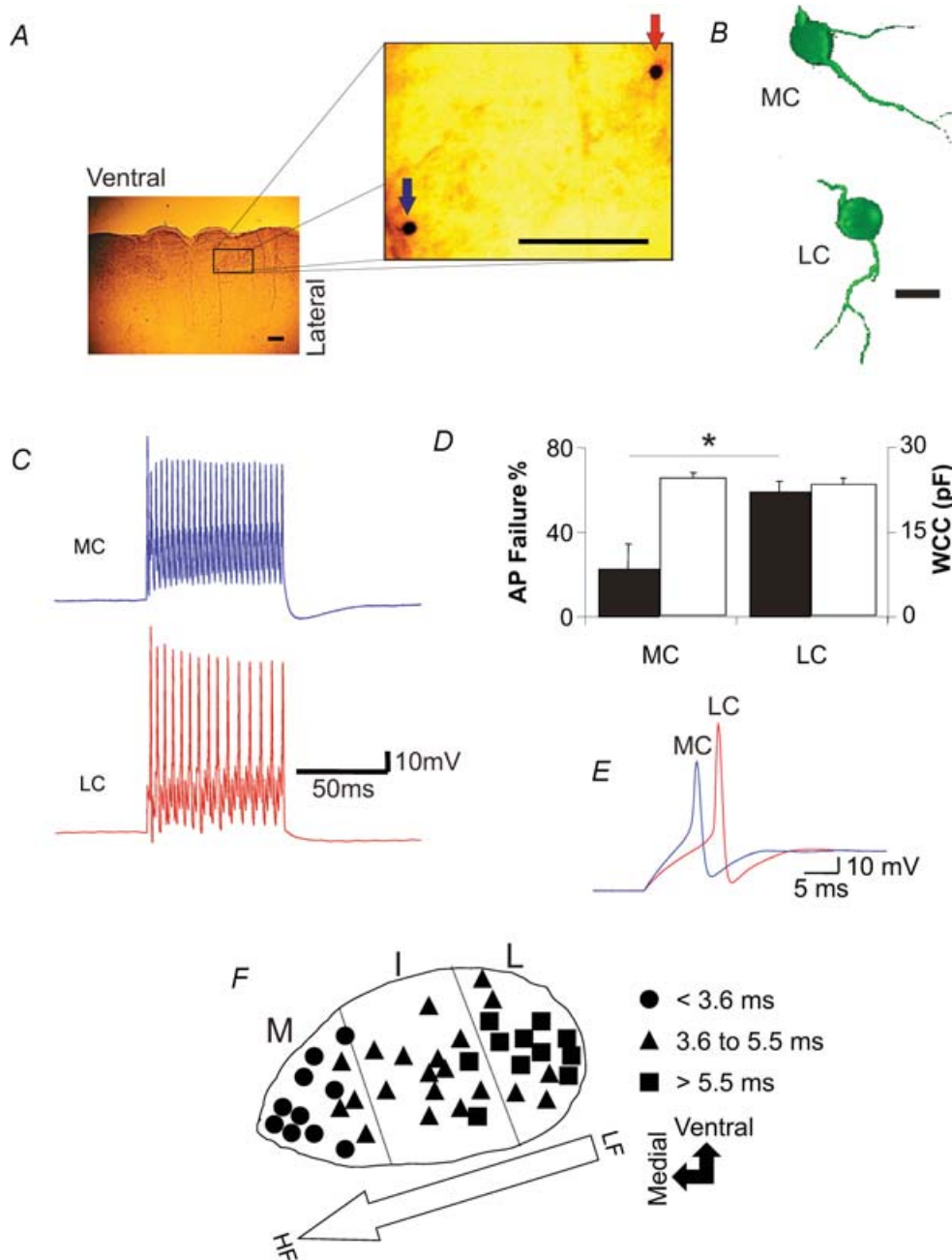
Figure 1. MNTB neurones from normal hearing mice exhibit a medio-lateral gradient of firing properties and delays

A, photomicrographs of a transverse brainstem slice showing two neurobiotin-labelled MNTB neurones from which whole-cell recordings had previously been obtained. Scale bar, 200 μm. *B*, high magnification images of the medial cell (MC) and lateral cell (LC). Scale bar, 20 μm. *C*, action potential responses to current pulse trains (0.5 ms, 2 nA, 600 Hz), for a medially located cell (blue trace) and a lateral cell (red). *D*, summary bar chart showing that medial cells in the MNTB exhibit a much lower failure rate of action potential responses to high-frequency (600 Hz) current pulses than lateral cells (filled bars). Whole-cell capacitance (WCC) measurements showed no medio-lateral differences between cells (open bars). *E*, examples of two MNTB neurones showing that the delay to action potential generation following a depolarizing current step (150 pA) is greater for lateral cells than for medial cells. *F*, location of MNTB neurones (M, medial; I, intermediate; L, lateral) in the MNTB (outline) reveals a medio-lateral gradient of action potential delays to depolarizing current steps (150 pA). Cells (total = 42) were divided into 3 groups corresponding to the delay ranges indicated. Arrow indicates the tonotopic organization of the MNTB from lower frequency (LF) to higher frequency (HF) cells.

temperature (comparing medial and lateral cell pairs in the same slices – see Fig. S1 in Supplemental Material). Transients simulating large calyceal synaptic conductance changes were also injected in order to assess whether the gradient of delays was maintained in the presence of strong synaptic inputs. There was a significant difference in the delay (to peak) of the action potential between medial cells (MC, 1.65 ± 0.10 ms) *versus* lateral cells (LC, 1.82 ± 0.10 ms; $P < 0.05$, $n = 10$).

We next investigated the mechanisms underlying the tonotopic gradient of membrane properties.

Tonotopic gradient of whole-cell currents in response to voltage-clamp steps

Voltage-clamp recordings were made of whole-cell currents in response to 100 ms duration voltage steps from -74 mV to 40 mV in the presence of $CdCl_2$ and TTX to block voltage-dependent calcium and sodium currents, respectively. Outward currents displayed a large non-inactivating component and a smaller inactivating component. Whole-cell current–voltage relationships are shown in Fig. 2. Figure 2A shows examples of whole-cell currents for an MC, an IC and an LC. There is an obvious

relationship between the amplitude of the whole-cell currents and the location of cells, with the most medial cells exhibiting the largest currents. Figure 2B shows summary data of I–V plots for 30 MNTB neurones, for steady-state (SS) and tail currents (T). A clear relationship is evident from these plots, with the most medial cells exhibiting the largest steady-state and tail currents. The steady-state current for MCs at 40 mV was 7.0 ± 0.8 nA, 5.0 ± 0.8 nA for ICs and 3.2 ± 0.6 for LCs ($n = 30$; ANOVA, $P < 0.01$). Tail currents, measured 1.5 ms after the end of the voltage step, also differed significantly (for 40 mV: 922 ± 123 pA for MCs, 677 ± 95 pA for ICs and 301 ± 56 pA for LCs; $n = 36$, $P < 0.05$, ANOVA). In order to obtain the amount of current that inactivates, we also measured the amplitude at the peak of the current trace and subtracted the steady-state current. Maximal inactivating currents for MC, IC and LC did not differ significantly (1.2 ± 0.1, 1.1 ± 0.1 and 0.9 ± 0.1 nA, respectively, $n = 36$). Inactivation time constants also did not show any significant difference (8.1 ± 1.0, 7.5 ± 1.0 and 7.5 ± 1.0 ms for MC, IC and LC, respectively, $n = 36$). We next isolated high- and low-threshold potassium currents from whole-cell currents using pharmacological blockers.
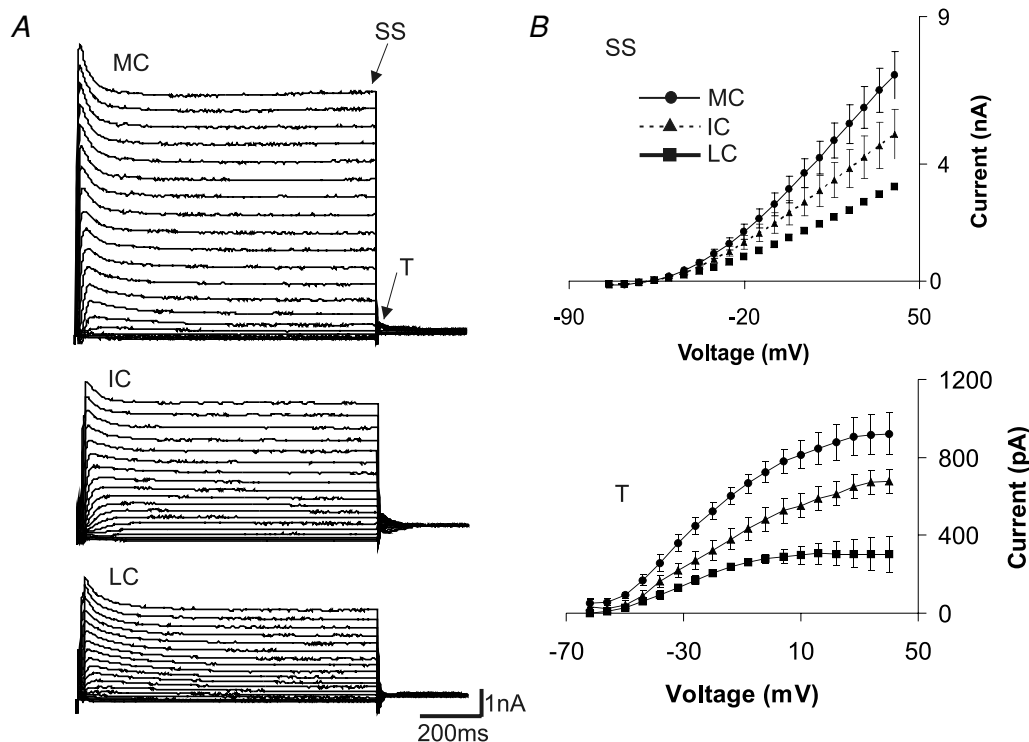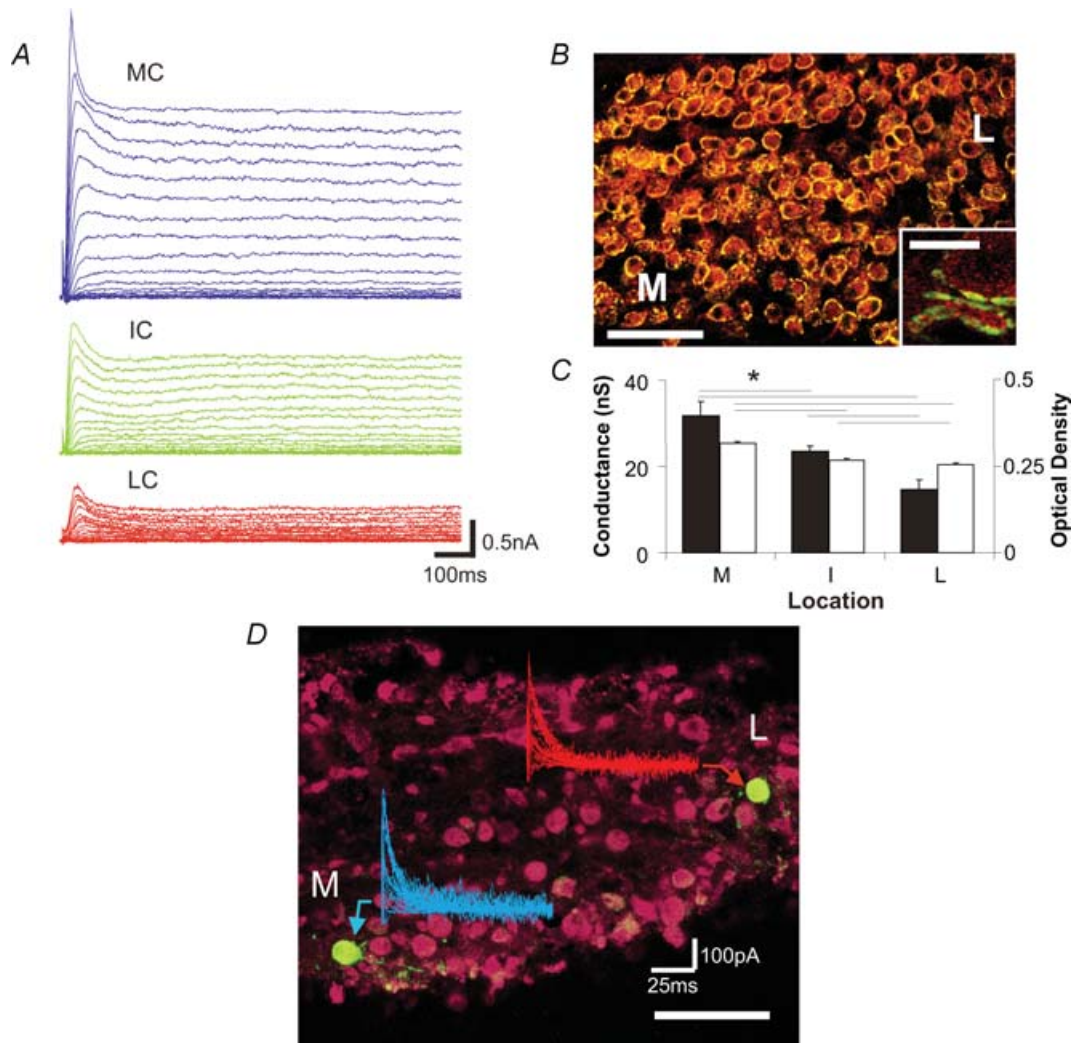

Figure 2. MNTB neurones exhibit a medio-lateral gradient of current amplitudes in response to depolarizing voltage steps
A, voltage-clamp recordings of whole-cell currents in response to 100 ms duration voltage steps from -74 mV to 40 mV. Examples of whole-cell currents for a medial cell (MC), an intermediate cell (IC) and a lateral cell (LC). B, summary data of I–V plots for 30 MNTB neurones, for steady-state (SS) and tail currents (T), see arrows in A. MC, medial cells; IC, intermediate cells; LC, lateral cells.

Tonotopic gradient of high-threshold K$^+$ currents and Kv3 immunoabelling

TEA (1 mM) was added to the bath to block high-threshold voltage-dependent K$^+$ currents (at this concentration, TEA did not affect low-threshold voltage-dependent currents; data not shown). Examples of subtracted traces for an individual MC, an IC and a LC are shown in Fig. 3*A*. Time constants and maximal conductances were obtained by digital subtraction of currents recorded before and after addition of 1 mM TEA. In order to avoid errors caused by series resistance (R_S), only traces where R_S changed less then 500 KΩ (before and after TEA addition) were analysed ($n = 5$ for each group – MC, IC and LC). The maximum conductances obtained by the formula $\bar{g} = I/(V - V_K)$ (where I is the current, V is the potential and V_K is the K$^+$ reversal potential) for TEA-sensitive currents for MC, IC and LC were 32.0 ± 1.5, 23.0 ± 0.6 and 15.0 ± 1.0 nS ($P < 0.01$, ANOVA, Fig. 3*C*, filled bars). There was a significant correlation between

Figure 3. High-threshold potassium currents exhibit a medio-lateral gradient in the MNTB
A, examples of TEA-subtracted traces for an individual MC, an IC and a LC. Time constants and maximal conductances were obtained by digital subtraction of currents recorded before and after addition of 1 mM TEA. *B*, Kv3.1b channel immunolabelling (red) is present in the cytoplasm and surface membrane of principal neurones, and in glutamatergic, VGLUT1-immunoreactive (green) presynaptic terminals. Inset shows overlap (yellow) of Kv3.1b and VGLUT1 labelling in presynaptic terminals, as well as punctate postsynaptic surface membrane staining. Optical density measurements of postsynaptic cell labelling shows a significant correlation with location (open bars in *C*). *C*, maximal (TEA-subtracted) conductance exhibits a significant correlation with medio-lateral location (filled bars). *D*, I_A currents (blue and red traces) obtained by applying consecutive voltage steps preceded by different holding voltages (see Methods) do not exhibit a medio-lateral gradient. Arrows indicate the two cells in the same MNTB slice from which the recordings were made. Kv 3.4 immunoreactivity (red) is relatively similar in medial and lateral neurones. Calibration bars in *B*, 100 μm; inset, 10 μm; and in *D*, 100 μm.

medio-lateral location and high-threshold potassium conductance, with the most medial cells exhibiting the largest conductance. Activation time constants were obtained by fitting $A[(e^{-t/\tau_n})^3 + e^{-t/\tau_p}]$ to the activation phase of the current recording, where A is the scaling factor (amplitude), τ_n is the fast activation time constant and τ_p is the slow activation time constant. Mean τ_n values for a 10 mV voltage step were smaller for MCs and ICs (1.30 ± 0.05 and 1.8 ± 0.3 ms, respectively) than LCs (2.2 ± 0.3 ms, $P < 0.03$). Inactivation time constants did not differ between MC, IC and LC.

Immunolabelling of Kv3 potassium channels was performed to provide insight into the subtypes of potassium channels which may contribute to the observed high-threshold potassium currents. Kv3.1b gene transcripts are expressed in MNTB principal cells and in presynaptic glutamatergic terminals (Fig. 3*B*). Immuno-staining intensity in principal cells was significantly higher in medially located neurones than in laterally located neurones, in accordance with the gradient of TEA-sensitive currents. Optical density measurements showed a significant correlation with location, as illustrated in Fig. 3*C* (open bars).

Other members of the Kv3 family, including Kv3.4 channels, are known to produce transient K$^+$ currents

(I_A). The contribution of I_A currents to high-threshold 1 mM TEA-sensitive currents was further investigating by applying consecutive voltage steps preceded by different holding voltages (see Methods). Differences in maximum I_A currents between MCs and LCs were not significant (407.96 ± 69.40 *versus* 415.67 ± 61.10 pA, respectively; $n = 14$, $P = 0.29$; Fig. 3*D*). Immunolabelling showed that postsynaptic Kv3.4 immunoreactivity was not significantly different across the medio-lateral axis of the MNTB (Fig. 3*D*).

Low-threshold voltage-dependent K$^+$ currents and tonotopicity

We used α-dendrotoxin (DTX) in 24 cells to block low-threshold voltage-dependent currents from other currents using the same protocol as for high-threshold currents. Figure 4*A* illustrates examples of current responses to voltage steps of the subtracted (DTX sensitive) components, for an MC, IC and LC. Maximal DTX-sensitive conductances did not differ between MCs, ICs and LCs (11.2 ± 1.3, 8.2 ± 0.7 and 9.3 ± 1.0 nS, respectively, $n = 24$). The activation parameters for the DTX-sensitive currents were calculated by fitting a Boltzmann function ($\bar{g}/(1 + e^{(V_{1/2}-V)/k})$, where $V_{1/2}$ is the
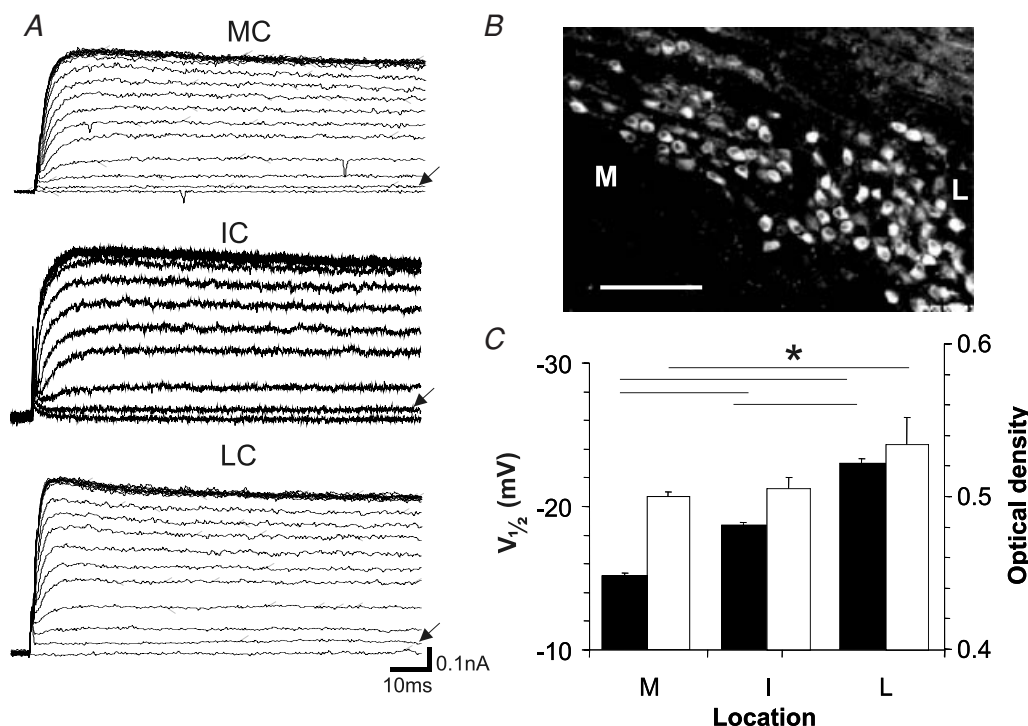
Figure 4. Low-threshold voltage-dependent K$^+$ channels exhibit a medio-lateral gradient in the MNTB
A, examples of α-dendrotoxin (DTX)-subtracted currents in response to voltage steps, for a MC, IC and LC. *B*, immunolabelling of Kv1.1 channels. Optical density measurements show a clear correlation between location and labelling intensity (filled bars in *C*). *C*, half-activation voltage ($V_{1/2}$) of the DTX-sensitive conductance *versus* location in the MNTB (open bars, see text for explanation). Calibration bar in *C*, 100 μm.

half-activation voltage and k is the slope factor) to the DTX-sensitive conductance *versus* voltage relationships. $V_{1/2}$ and k values did not differ significantly between MC and IC, but there were significant differences ($P = 0.03$) for those variables between MC and LC ($V_{1/2}$: -20.7 ± 0.4, -21.3 ± 0.7 and -24.3 ± 2 mV, respectively; Fig. 4C; k: 10.0 ± 0.4, 10.8 ± 0.8 and 11.5 ± 0.4 mV, respectively).

Two low-threshold potassium channels that confer DTX sensitivity, Kv1.1 and Kv1.2, are expressed in MNTB neurones and presynaptic axons, whilst a third, Kv1.6, is less clearly expressed. Figure 4B illustrates immunoreactivity for Kv1.1 channels. Optical density measurements show a clear correlation between location and labelling intensity (Fig. 4C). Postsynaptic Kv1.1 immunoreactivity is significantly higher in lateral MNTB neurones. No gradients were observed for Kv1.2 and Kv1.6 immunoreactivity.

Hyperpolarization-activated currents show an inverse tonotopic gradient to total voltage-gated potassium currents

MNTB neurones exhibit hyperpolarization-activated currents. We therefore tested if I_h magnitudes are different between MCs, ICs and LCs in the MNTB by applying hyperpolarizing voltage steps (500 ms duration from -60 to -30 mV in 5 mV decrements) in 18 cells without and with ZD7288 to block I_h. Figure 5A illustrates subtracted (ZD7288-sensitive) currents for an MC, an IC and an LC. In control conditions (with no ZD7288 in the bath), maximal currents for MCs, ICs and LCs were, respectively, -0.8 ± 0.1, -0.6 ± 0.6 and -0.4 ± 0.1 nA, ANOVA, $P = 0.04$). Addition of ZD7288 to the bath blocked 56 ± 9, 44 ± 10 and $25 \pm 2\%$ of the current for MC, IC and LC, respectively (significant differences were found between MC and LC, and IC and LC,
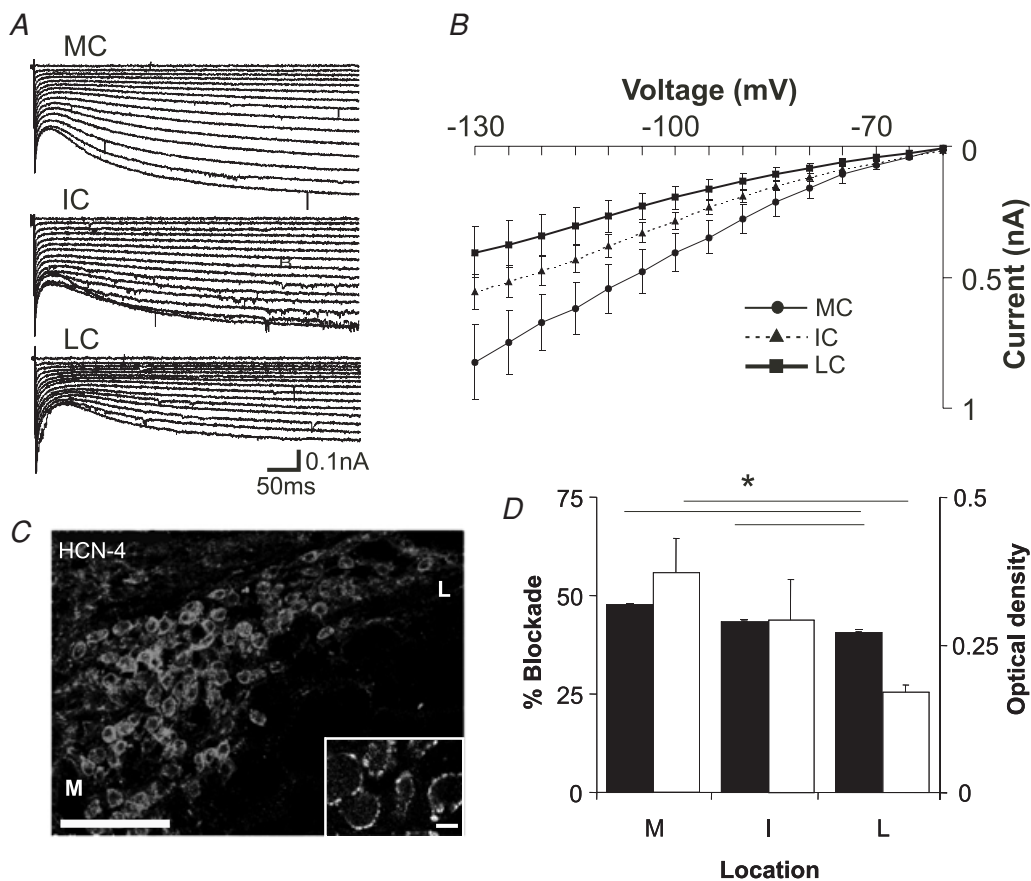
Figure 5. Hyperpolarization-activated channel expression and currents exhibit a medio-lateral gradient
A, examples of hyperpolarization-activated currents (ZD7288-subtracted) for a medial, an intermediate and a lateral cell in the MNTB. *B*, summary of *I–V* relationships for hyperpolarizing voltage steps for MC, IC and LC. *C*, immunoreactivity of HCN4 channels is expressed in the surface membrane of MNTB neurones, and is often postsynaptic to VGLUT1-immunoreactive terminals (inset). Optical density measurements show that medial neurones display higher levels of immunoreactivity than lateral neurones (open bars in *D*). *D*, percentage block (ZD7288) of hyperpolarization-activated currents according to medio-lateral location (filled bars). Calibration in *C*, 100 μm.

$P = 0.04$ and $P < 0.04$, respectively). Figure 5*B* summarizes the *I–V* relationships for MNTB neurones for the ZD7288-sensitive currents. It is clear that the most medial cells exhibit the largest hyperpolarization-activated currents. We next used immunolabelling to analyse the distribution of three of the HCN channels underlying I_h, namely, HCN1, HCN2 and HCN4. The HCN1 isoform is particularly highly expressed in the soma and dendritic membranes of neurones in the superior olivary complex and ventral cochlear nucleus, but is expressed at much lower, barely detectable, levels in MNTB principal neurones. HCN1 in the MNTB is clearly present in presynaptic glutamatergic terminals, including the calyx of Held. HCN2 is weakly expressed in MNTB principal neurones, primarily in the form of cytoplasmic labelling, with accumulation near or at the cell surface. HCN4 is expressed in the soma of MNTB neurones and is localized in small surface membrane punctate clusters, some of which are apposed to VGLUT1-immunoreactive presynaptic terminals, as well as in the cytoplasm (Fig. 5*C*).
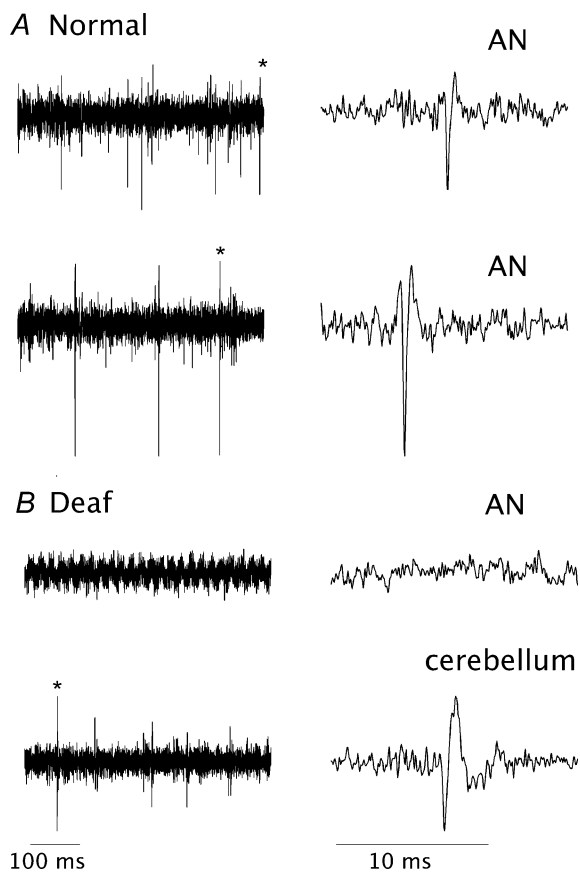
Figure 6. Recordings from the auditory nerve *in vivo* show a lack of spontaneous activity in *dn/dn* mice
A illustrates single unit recordings from the auditory nerve (AN) in a normal CBA mouse (12 days postnatal). *B* shows a lack of auditory nerve activity in a *dn/dn* mouse (12 days postnatal). As a control, single unit activity was readily recorded in the cerebellum of this *dn//dn* mouse (cerebellum).

The level of cytoplasmic immunoreactivity is higher in medial *versus* lateral neurones in MNTB. Since the antibodies against each HCN subunit were produced in the same species, we did not perform dual labelling with the channel antibodies to establish the degree of co-localization; nevertheless, the consistent cellular staining with each antibody across the breadth of the nucleus indicates that the vast majority of, if not all, MNTB principal cells co-express each of the three subunits. Moreover, HCN4 appears to be the channel isoform with the most clearly defined postsynaptic membrane localization.

Deaf mice lack a tonotopic gradient of action potential delays and whole-cell membrane currents

Having revealed the tonotopic gradients of membrane currents in normal mice, we next investigated the question of how these tonotopic gradients are established. We used congenitally deaf *dn/dn* mice to examine the potential role of auditory nerve activity during development. Since spontaneous auditory nerve activity occurs in normal mice before ear canal opening at around 12 days, we first needed to verify that *dn/dn* mice lack spontaneous auditory nerve activity. Experiments were performed using *in vivo* single and multi-unit recording of the auditory nerve in both normal and congenitally deaf mice from 1 to 2 weeks postnatal age. Spontaneous action potentials were readily recorded in normal mice ($n = 5$), but the auditory nerve was silent in all *dn/dn* mice ($n = 5$; Fig. 6). Control experiments of single unit recording in cerebellar cortex verified that activity could be recorded in both normal and deaf mice (Fig. 6*B*). Whole-cell current-clamp recordings of MNTB neurones showed that deaf mice lacked the medio-lateral gradient of action potential delays demonstrated in normal mice in response to depolarizing current pulses (Fig. 7*A* and *B*). In contrast to normal mice, there was no statistically significant difference between the delays in MC, IC or LC (current step 150 pA, $n = 21$, $P > 0.05$; Fig. 7*B*). Voltage-clamp recordings of whole-cell currents in response to depolarizing voltage steps also showed a lack of a medio-lateral gradient of amplitudes, in contrast to normal mice. Figure 7*C* illustrates examples of current responses to voltage steps for a MC, an IC and a LC from deaf mice. Figure 7*E* shows summary *I–V* relationships for MC, IC and LC from deaf mice, demonstrating no significant differences ($n = 21$, $P > 0.05$), in contrast to normal mice (compare with Fig. 2*B*). Tail currents measured at 40 mV in deaf mice MC, IC and LC were, respectively, 912 ± 120, 909 ± 115 and 913 ± 189 pA ($n = 21$, $P > 0.05$). Immunoreactivity for Kv channels was examined in deaf mice, and found to lack a medio-lateral gradient, in contrast to normal mice. Figure 7*D* illustrates DAB immunoreactivity for Kv3.1b channels in normal and deaf mice. Optical density

measurements, which showed a gradient in the MNTB of normal mice (see Fig. 3*B* and *C*), did not exhibit a gradient in the MNTB of deaf mice.
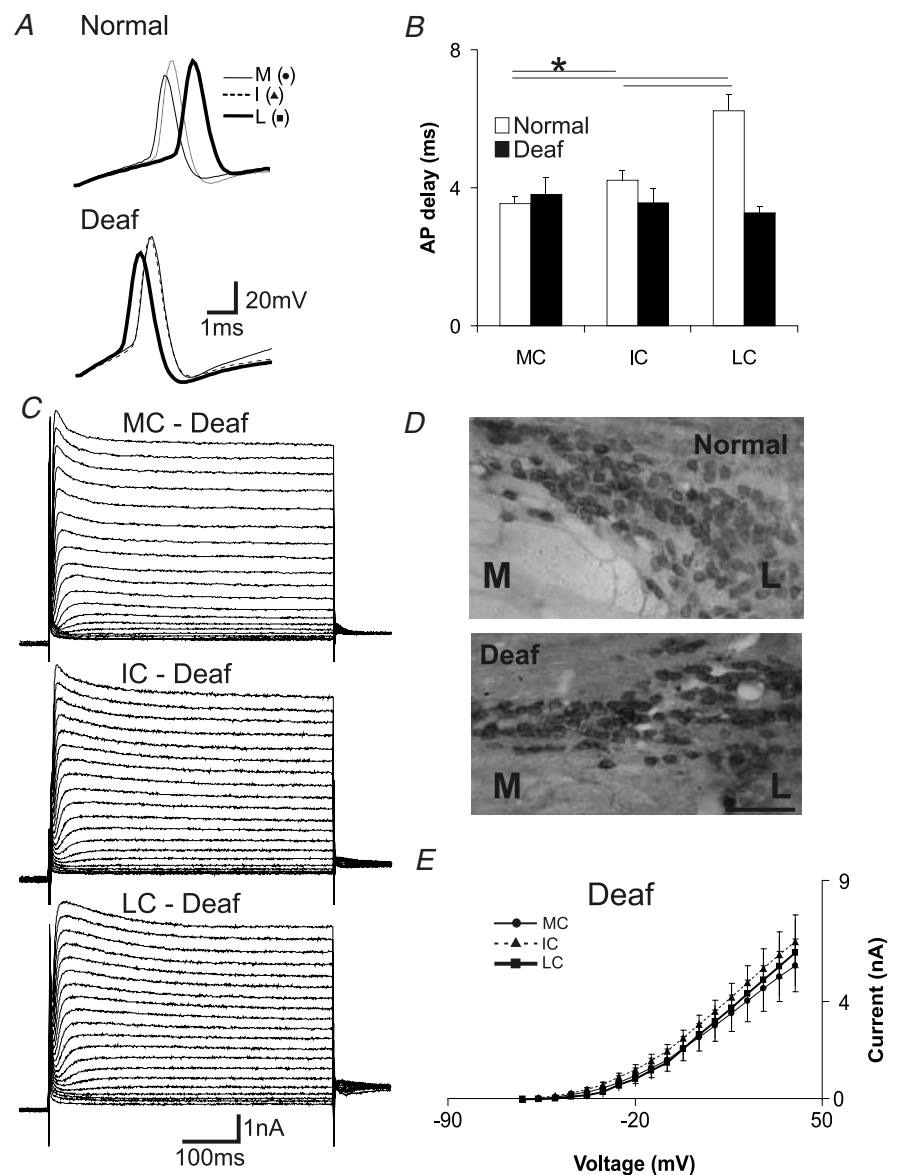
Deaf mice lack a medio-lateral gradient of hyperpolarization-activated currents

Following our observation of a medio-lateral gradient of hyperolarization-activated currents in the MNTB of normal mice, we investigated I_h and HCN immuno-labelling in deaf mice. Figure 8*A* illustrates examples of I_h (ZD7288-subtracted) for a MC, an IC and a LC in the MNTB of deaf mice. Summary data shown in Fig. 8*B* illustrate no significant differences in the magnitude of the ZD7288-sensitive current (% blockade) between medial (M), intermediate (I) and lateral (L) cells in deaf

mice ($n = 21$, $P > 0.05$; compare with Fig. 5*D* for normal mice). Similarly, the gradient demonstrated for immuno-reactivity of HCN4 channels in the MNTB of normal mice (see Fig. 5*D*), is absent in deaf mice (Fig. 7*B* and *C*; $n = 21$, $P > 0.05$).

Modelling shows that the tonotopic gradient of MNTB firing properties in normal mice is explained a combination of Kv and I_h channel gradients

Figure 9*A* shows a schematic summary of our results in the MNTB of normal and deaf mice. Current amplitudes and immunoreactivity reveal a positive medio-lateral gradient for Kv1.1 channels and a negative gradient for Kv3.1 and HCN4 channels in normal mice, and a lack of gradient for all these channels in deaf mice.

**Figure 7. Medio-lateral gradients of delays and whole-cell currents are absent in deaf mice**

A, examples of MC, IC and LC APs in normal and deaf mice (200 pA current step). *B*, summary of AP delays in response to a 200 pA current step. Note the lack of correlation with position in deaf mice (filled bars), in contrast to normal hearing mice (open bars) *C*, example of voltage-clamp recordings of whole-cell currents in response to 100 ms duration voltage steps from −74 mV to 40 mV of a MC, IC and LC of a deaf mouse. *D*, examples of biotin immunoreactivity of Kv3.1 channels in a normal and deaf mouse. *E*, summary data of *I–V* plots of depolarizing current amplitudes (see Fig. 6*C*) from MCs, ICs and LCs from the MNTB of deaf mice.

Incorporating the measured currents in a Hodgkin-Huxley (H-H) model of MNTB neurones (see Methods) shows that the differences in firing properties exhibited by MNTB neurones can be accounted for by differences in these currents. Figure 9*B* illustrates the responses of MNTB neurones to 400 Hz current pulses, showing that medial cells are more capable of following this high-frequency input than intermediate or lateral cells. Interestingly, MNTB neurones in deaf mice are more capable of following high-frequency inputs than intermediate or lateral cells in normal mice. Figure 9*D* illustrates that the medio-lateral gradient of action potential delays to current pulses found in normal mice is replicated in the H-H model based on measured current differences.

Discussion

Tonotopic organization of cell properties begins in the cochlea itself, and is continued into the central auditory nuclei. In the chick, Pantelias *et al.* (2001) have shown that

there is a tonotopic organization of potassium currents in cochlea hair cells. Our electrophysiological results show that in normal hearing mice there are distinct medio-lateral gradients of voltage-dependent currents in mouse MNTB neurones, and these gradients correlate with optical density measurements of immunoreactivity for underlying channel types. The gradients are specific for particular channels: Kv1-mediated low-voltage-activated potassium currents are greater in more laterally located cells, whereas high-threshold potassium currents and hyperpolarization-activated currents are greater in more medial cells. In addition, the mean difference between low- and high-threshold-activated potassium currents in deaf and normal mice can be seen by comparing the whole-cell current–voltage relationships in Figs 2 and 7, which show that, on average, low-threshold potassium currents are smaller in deaf mice (see also Leao *et al.* 2004*a*) and high-threshold potassium currents are greater in deaf mice. The high-threshold potassium current tonotopic data agree with previous evidence in the rat MNTB
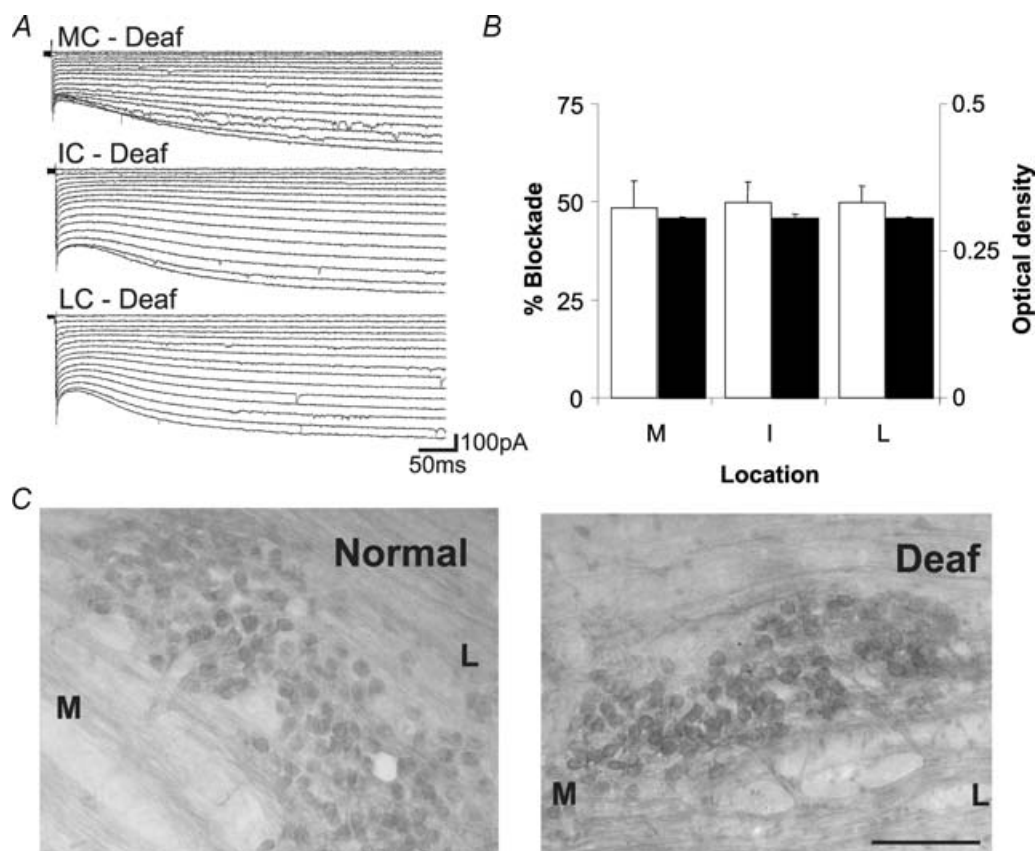

Figure 8. Deaf mice lack a medio-lateral gradient of hyperpolarization-activated currents and HCN immunoreactivity
A, examples of I_h for a MC, IC and LC in the MNTB of a deaf mouse. *B*, summary data of the percentage blockade by ZD7288 of the hyperpolarizing currents in deaf mice (open bars) and the optical density of HCN4 immunoreactivity in deaf mice (filled bars; see Fig. 7*C*). *C*, examples of HCN-4 immunoreactivity in the MNTB of normal and deaf mice. Calibration bar, 100 μm.

showing that Kv3.1 immunolabelling is stronger in more medial cells (Li *et al.* 2001). However, Brew & Forsythe (2005) found that Kv1-mediated currents are largest in the most medial cells of the rat MNTB, which is opposite to our result in the mouse MNTB (although they found a similar gradient for an intermediate voltage-threshold potassium current). This difference may be a species difference (rat *versus* mouse). Our results in the mouse MNTB

show that the maximum dendrotoxin-sensitive potassium conductance is not significantly different for medial *versus* lateral cells, and the gradient of current amplitudes is generated by differences in the voltage-activation curves for these channels. We found that the half-activation voltage for low-threshold potassium currents is more negative in the most lateral cells, whereas Brew & Forsythe (2005) found the opposite result in the rat MNTB. One
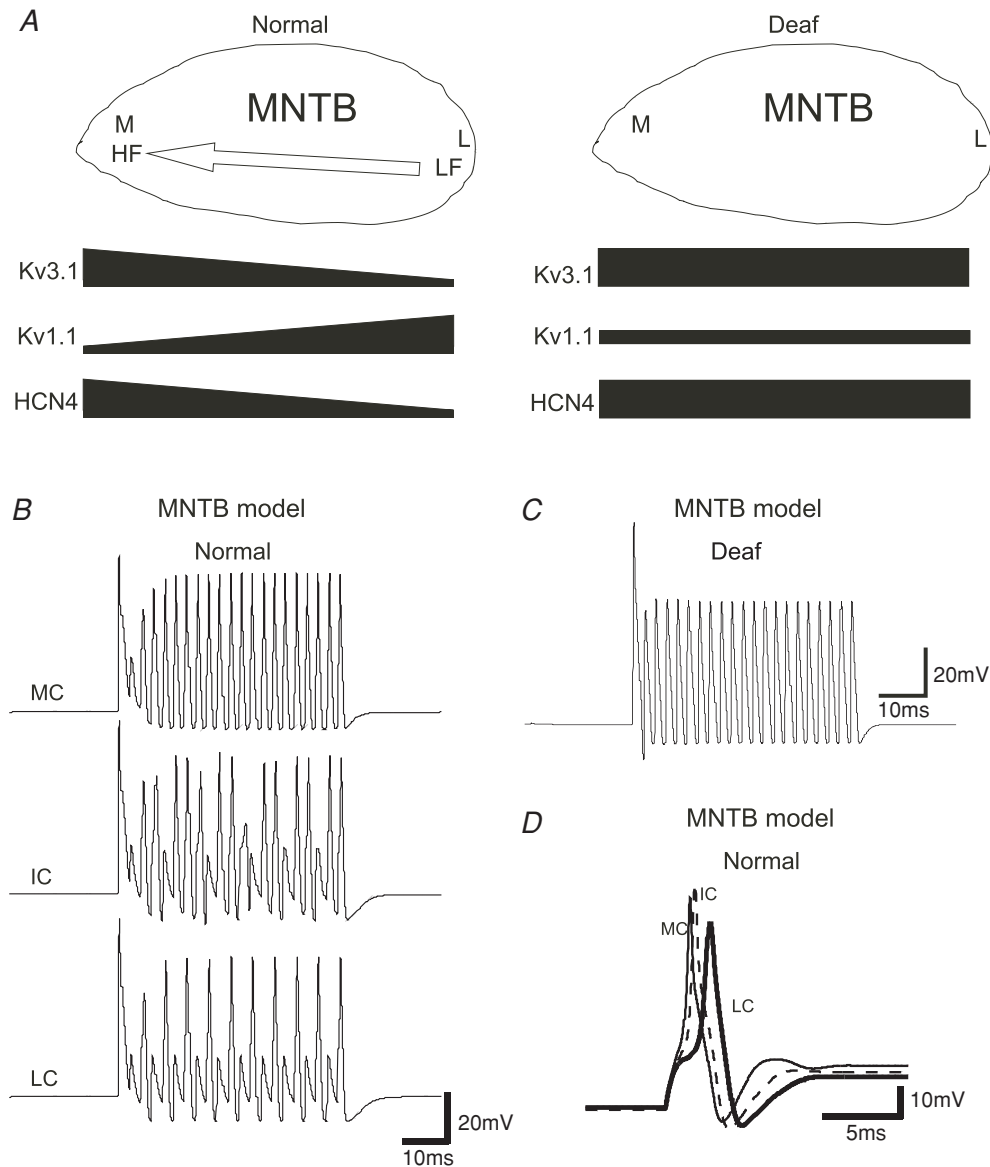
Figure 9. Schematic summary of voltage-dependent channels along the MNTB tonotopic axis for normal and deaf mice

A, in normal mice, Kv3.1 and HCN4 channels are more prominent medially, in contrast to the opposite gradient shown by Kv1.1 channels. Gradients for these channels are not observed in deaf mice. HF, high frequency; LF, low frequency. *B*, action potential generation in a model simulation of a MC, an IC and a LC in response to simulated trains of calyceal EPSPs (400 Hz). *C*, response of a model of an MNTB cell to the same stimulus. *D*, MC, IC and LC model responses to a 200 pA current step. Note that the combination of high- and low-threshold voltage-dependent potassium channels and I_h channels simulates the different delays observed experimentally between MCs, ICs and LCs in the MNTB of normal hearing mice.

possibility is that there is a medio-lateral gradient in the relative expression of Kv1 channel subtypes, which exhibit different voltage–activation relationships (Hopkins *et al.* 1994; Brew & Forsythe, 2005). Interestingly, Barnes-Davies *et al.* (2004) showed that in the rat lateral superior olive (LSO), the tonotopic gradient of Kv1.1 channels is the same as our result in the mouse MNTB, with expression being greatest in the low characteristic frequency neurones. Our immunolabelling shows that there is a gradient of Kv1.1 immunoreactivity which matches the gradient of current amplitudes, with the lateral cells displaying larger currents and more intense immunoreactivity. We found no gradient in Kv1.2 immunoreactivity.

Our experimental and modelling results show that the graded combination of voltage-dependent currents endows MNTB neurones with firing properties appropriate for their tonotopic location within the nucleus. The most medially located neurones in the MNTB are able to respond to higher frequency synaptic inputs with fewer action potential failures than lateral neurones. MNTB neurones usually respond to synaptic input with a single action potential, due in large part to the presence of dendrotoxin-sensitive low-threshold potassium currents (Dodson *et al.* 2002). A small low-threshold potassium current results in multiple firing, whereas a large low-threshold potassium current prevents a neurone from being able to fire at high frequencies. Our results show that the most medial (higher frequency) MNTB neurones exhibit low-threshold potassium currents with an activation threshold at more depolarized potentials than those currents in lateral neurones, which would allow these neurones to discharge at higher frequencies. The firing properties are also influenced by hyperpolarization-activated currents (Leao *et al.* 2005). The study of Leao *et al.* (2005) reported that hyperpolarization-activated currents are larger, on average, in congenitally deaf mice than in control mice. Our present results show there is a gradient of this current in the MNTB of control mice and that, furthermore, this gradient is in the opposite direction to low-threshold potassium currents within the MNTB. Taken together, these results suggest that auditory activity in normal animals down-regulates the expression of HCN channels, with expression in lateral cells more suppressed than medial cells in the MNTB. Our experimental and modelling results show that there is an interplay between hyperpolarization-activated currents and potassium currents, and the balance provides MNTB neurones with firing properties that vary along the tonotopic axis. Neuronal excitability, and hence action potential generation, depends on a number of factors, including resting membrane potential, resting membrane conductance and the current–voltage relationships of voltage-dependent conductances. Because of the differences in activation kinetics of low-threshold potassium currents and I_h, differences in the proportion of these currents, due to the total number of channels or differences in their current–voltage relationships, will change the kinetics of the response of the neurone. In the MNTB, the combination of gradients of low-threshold potassium currents and I_h results in a gradient of membrane excitability and delays to action potential initiation. For example, low-threshold potassium channels contribute little to the resting conductance of medial MNTB cells, while this contribution is more prominent in lateral cells. A low-threshold potassium conductance may 'shunt' inputs, causing lateral cells to fire later than medial cells. On the other hand, I_h channels lower the input resistance of medial cells, which compensates for the lack of a resting potassium conductance in these cells. High-threshold potassium currents are also graded along the tonotopic axis of the MNTB. These currents serve to increase the rate of repolarization of the action potential and reduce its duration (Wang *et al.* 1998). It is appropriate that the most medial cells in the MNTB, which are required to fire at the highest frequencies, exhibit the greatest amplitude high-threshold potassium currents.

A tonotopic gradient of delays in the MNTB

An interesting consequence of the gradient of combinations of membrane currents in the MNTB is that this produces a medio-lateral gradient of time delays of action potential initiation in response to injected current. Reed & Blum (1990) developed a model for interaural level difference (ILD) azimuth processing based on 'threshold' lines, but no anatomical evidence for such an arrangement has been forthcoming (see also Fitzgerald *et al.* 2001; Yin, 2002). The greater fidelity of medial cells in following their inputs could translate into a greater post-synaptic inhibition to the LSO. Moreover, shorter delays in the anteroventral cochlear nucleus (AVCN)-MNTB pathway result in earlier (and perhaps coincident) inhibition to the LSO, therefore being more likely to shunt ipsilateral excitation to LSO cells. A previous study suggests that precisely timed inhibition, most likely from the MNTB, provides the basis for computation of sound localization in the MSO through temporal cues (Brand *et al.* 2002; Grothe, 2003; McAlpine & Grothe, 2003; for discussion on delay times in auditory brainstem pathways, see Fitzgerald *et al.* 2001; Paolini *et al.* 2004). Brand *et al.* (2002) showed that in the MSO, there is a strong inverse correlation between best ITD and best CF, and that this tonotopic arrangement of best ITDs in the MSO is due to precisely timed input from the MNTB. Our results suggest that MNTB neurones could provide an assembly of delay lines to produce graded timing of inhibition to MSO neurones, with low CF neurones generating the greatest delays. The delays depend on the magnitude of

the injected (or synaptic) current, and it could be argued that the postsynaptic current generated at the calyx of Held is so large that the difference in delays between medial and lateral cells may be very small. However, our dynamic clamp results show that there is a small but significant difference (0.2 ms) between medial and lateral cells in the delay to action potential generation following large simulated synaptic conductance changes. Moreover, while the synaptic current is large (several nanoamps) following the first stimulus in a train, there is a rapid depression to very small currents after only three or four stimuli (Oleskevich *et al.* 2004; Youssoufian *et al.* 2005). In any case, our results show that the intrinsic membrane properties of MNTB neurones, specifically potassium and hyperpolarization-activated currents, provide a source of time delays. Although the functional significance of these time delays is speculative, our results provide evidence that delay lines do not require morphological differences (e.g. axonal length), as a systematic gradient of delays can be assembled by different ion channel densities.

Spontaneous activity during development is necessary for the regulation of membrane properties

Our results show that the gradient of voltage-dependent currents which exist in the MNTB of normal hearing mice are absent in congenitally deaf *dn/dn* mice. Our *in vivo* recordings demonstrate that there is no detectable spontaneous activity in the auditory nerve even prior to ear canal opening in *dn/dn* mice, which has allowed us to address the role of spontaneous activity *versus* sound-induced activity in shaping auditory pathways (Friauf & Lohmann, 1999; see Pienkowski & Harrison, 2005). The use of this congenitally deaf mouse provides a valuable alternative to previous studies using cochlea ablation to eliminate auditory nerve input (which inevitably eliminates the cochlea nerve itself; see Kandler & Gillespie, 2005). Previous studies have provided evidence for a role of activity in regulating the properties of auditory neurones. Lu *et al.* (2004) demonstrated activity-dependent regulation of Kv1.1 and Kv3.1 channels in the avian nucleus magnocellularis following removal of the cochlea, and von Hehn *et al.* (2004) showed that the tonotopic gradient of Kv3.1 channels is altered in hearing-impaired mice. Our results show a lack of a tonotopic gradient of membrane currents in *dn/dn* mice around the time of ear canal opening. This provides strong evidence that spontaneous auditory nerve activity during development is a major determinant of the membrane properties of MNTB neurones, and the origin of the tonotopic gradient. In this context, it is interesting that globular bushy cells, which project to the MNTB, are preferentially innervated by auditory nerve fibres which exhibit high spontaneous firing rates (Liberman, 1991).

Conclusion

Our results have demonstrated a medio-lateral gradient of several voltage-activated membrane currents in an important auditory brainstem nucleus, the MNTB, which provides the basis for the tonotopic gradient of neuronal firing properties in this nucleus. Importantly, we have shown that normal spontaneous auditory nerve activity is necessary for establishing this tonotopic map during development. Our results also suggest that spontaneous activity during development in normal mice is responsible for the up-regulation of low-threshold potassium currents, and the down-regulation of high-threshold potassium currents and hyperpolarization-activated currents. The further study of brainstem auditory pathways offers much promise in the investigation of the mechanisms underlying activity-dependent expression of membrane channels in central neurones.

References

Barnes-Davies M, Barker MC, Osmani F & Forsythe ID (2004). Kv1 currents mediate a gradient of principal neuron excitability across the tonotopic axis in the rat lateral superior olive. *Eur J Neurosci* **19**, 325–333.

Bock GR, Frank MP & Steel KP (1982). Preservation of central auditory function in the deafness mouse. *Brain Res* **239**, 608–612.

Brand A, Behrend O, Marquardt T, McAlpine D & Grothe B (2002). Precise inhibition is essential for microsecond interaural time difference coding. *Nature* **417**, 543–547.

Brew HM & Forsythe ID (2005). Variation of potassium current amplitudes across the tonotopic axis of the rat medial nucleus of the trapezoid body. *Hear Res* **206**, 116–132.

Dodson PD, Barker MC & Forsythe ID (2002). Two heteromeric Kv1 potassium channels differentially regulate action potential firing. *J Neurosci* **22**, 6953–6961.

Fitzgerald JV, Burkitt AN, Clark GM & Paolini AG (2001). Delay analysis in the auditory brainstem of the rat: comparison with click latency. *Hear Res* **159**, 85–100.

Friauf E & Lohmann C (1999). Development of auditory brainstem circuitry. Activity-dependent and activity-independent processes. *Cell Tissue Res* **297**, 187–195.

Grothe B (2003). New roles for synaptic inhibition in sound localization. *Nature Rev* **4**, 540–550.

Hopkins WF, Demas V & Tempel BL (1994). Both N- and C-terminal regions contribute to the assembly and functional expression of homo- and heteromultimeric voltage-gated K^+ channels. *J Neurosci* **14**, 1385–1393.

Kandler K & Gillespie DC (2005). Developmental refinement of inhibitory sound-localization circuits. *TINS* **28**, 290–296.

Keats BJ & Berlin CI (1999). Genomics and hearing impairment. *Genome Res* **9**, 7–16.

Leao RN, Berntson A, Forsythe ID & Walmsley B (2004*a*). Reduced low-voltage activated K^+ conductances and enhanced central excitability in a congenitally deaf (*dn/dn*) mouse. *J Physiol* **559**, 25–33.

Leao RN, Oleskevich S, Sun H, Bautista M, Fyffe RE & Walmsley B (2004*b*). Differences in glycinergic mIPSCs in the auditory brain stem of normal and congenitally deaf neonatal mice. *J Neurophysiol* **91**, 1006–1012.

Leao RN, Svahn K, Berntson A & Walmsley B (2005). Hyperpolarization-activated (I) currents in auditory brainstem neurons of normal and congenitally deaf mice. *Eur J Neurosci* **22**, 147–157.

Li W, Kaczmarek LK & Perney TM (2001). Localization of two high-threshold potassium channel subunits in the rat central auditory system. *J Comp Neurol* **437**, 196–218.

Liberman MC (1991). Central projections of auditory-nerve fibers of differing spontaneous rate. I. Anteroventral cochlear nucleus. *J Comp Neurol* **313**, 240–258.

Lu Y, Monsivais P, Tempel BL & Rubel EW (2004). Activity-dependent regulation of the potassium channel subunits Kv1.1 and Kv3.1. *J Comp Neurol* **470**, 93–106.

McAlpine D & Grothe B (2003). Sound localization and delay-lines – do the mammals fit the model? *TINS* **26**, 347–350.

McAlpine D, Jiang D & Palmer AR (2001). A neural code for low-frequency sound localization in mammals. *Nat Neurosci* **4**, 396–401.

Mauk MD & Buonomano DV (2004). The neural basis of temporal processing. *Ann Rev Neurosci* **27**, 307–340.

Oleskevich S, Youssoufian M & Walmsley B (2004). Presynaptic plasticity at two giant auditory synapses in normal and deaf mice. *J Physiol* **560**, 709–719.

Pantelias AA, Monsivais P & Rubel EW (2001). Tonotopic map of potassium currents in chick auditory hair cells using an intact basilar papilla. *Hear Res* **156**, 81–94.

Paolini AG, Clarey JC, Needham K & Clark GM (2004). Fast inhibition alters first spike timing in auditory brainstem neurons. *J Neurophysiol* **92**, 2615–2621.

Paolini AG, FitzGerald JV, Burkitt AN & Clark GM (2001). Temporal processing from the auditory nerve to the medial nucleus of the trapezoid body in the rat. *Hear Res* **159**, 101–116.

Pienkowski M & Harrison RV (2005). Tone frequency maps and receptive fields in the developing chinchilla auditory cortex. *J Neurophysiol* **93**, 454–466.

Reed MC & Blum JJ (1990). A model for the computation and encoding of azimuthal information by the lateral superior olive. *J Acoust Soc Am* **80**, 1442–1453.

Rubel EW & Fritzsch B (2002). Auditory system development: primary auditory neurons and their targets. *Annu Rev Neurosci* **25**, 51–101.

Shepherd RK, Roberts LA & Paolini AG (2004). Long-term sensorineural hearing loss induces functional changes in the rat auditory nerve. *Eur J Neurosci* **20**, 3131–3140.

Taberner AM & Liberman MC (2005). Response properties of single auditory nerve fibers in the mouse. *J Neurophysiol* **93**, 557–569.

von Hehn CA, Bhattacharjee A & Kaczmarek LK (2004). Loss of Kv3.1 tonotopicity and alterations in cAMP response element-binding protein signaling in central auditory neurons of hearing impaired mice. *J Neurosci* **24**, 1936–1940.

Wang LY, Gan L, Forsythe ID & Kaczmarek LK (1998). Contribution of the Kv3.1 potassium channel to high-frequency firing in mouse auditory neurones. *J Physiol* **509**, 183–194.

Yin TCT (2002). Neural mechanisms of encoding binaural localization cues in the auditory brainstem. In *Integrative Functions in the Mammalian Auditory Pathway*, ed. Oertel D, Popper AN & Fay RR, pp. 99–159. Springer Verlag, New York, USA.

Youssoufian M, Oleskevich S & Walmsley B (2005). Development of a robust central auditory synapse in congenital deafness. *J Neurophysiol* **94**, 3168–3180.

Acknowledgements

Supplemental material

The online version of this paper can be accessed at:
DOI: 10.1113/jphysiol.2005.098780
http://jp.physoc.org/cgi/content/full/jphysiol.2005.098780/DC1
and contains supplemental material entitled:
Time delay gradient is significant at physiological temperature.

This material can also be found as part of the full-text HTML version available from http://www.blackwell-synergy.com